Check for updates

New approaches to three-dimensional positive electrodes enabling scalable high areal capacity†

Zhiyong Zhao, [ID] [a] Xiaowei Zhang, [ID] *[a] Peng Wang,[a] Ioanna Maria Pateli, [ID] [b] Hongyi Gao,[cd] Ge Wang*[c] and John T. S. Irvine [ID] *[ab]

Optimizing electrode architecture to enhance areal capacity is key to enabling greater capacity in batteries. Unfortunately, the cost and manufacturing techniques associated with innovative electrode designs have constrained their application. *In situ* powder infiltration is applied to integrate LiFePO$_4$ nanoparticles (LFP NPs) into highly porous aluminum networks (pAlN) in novel binder-free three-dimensional positive electrodes. The substrate assembled from porous Al wool and foams provides a continuous conductive skeleton. Combined *in situ* powder infiltration and solution impregnation enables direct anchoring of LFP onto the network, avoiding electrochemically inactive binder additives, whilst achieving excellent mechanical properties, high active material mass loading and good electronic/ionic conductivity. Due to the exquisite interface contact, the formed LFP/pAlN positive electrode exhibits superior areal capacity (6.56 mA h cm^{-2} at 0.55 mA cm^{-2}) and capacity retention (94.1%, at 2.32 mA cm^{-2} for 100 cycles). The new electrode structures maximize the functionality of available electrode materials, facilitating the integration of future chemistries into cost-effective and scalable devices.

1 Introduction

Seeking a paradigm shift in electrode design to deliver enhanced performance of secondary Li-ion batteries (LIBs) is of great importance for future energy storage.[1–3] In pursuit of high energy density and low-cost devices, advanced electrodes with high areal capacity have garnered significant attention.[4–7] LIB cells generally consist of active components, conductive materials and binders, which require careful adjusting of colloid chemistry and interface engineering. The active components (such as LiFePO$_4$ and LiCoO$_2$ systems) contribute to the energy density but account for about 40% of the total mass of commercial LIBs, thus seriously restricting their performance improvement and wide application.[8] The inactive materials such as current collectors, polymeric binders and conductive additives reduce energy density but are necessary for improving mechanical stability as well as current distribution.[9] Therefore, constructing thick electrodes to facilitate the high mass loading

of active materials and minimize inactive elements is considered a promising strategy for improving energy density and reducing total package costs.[10]

Increasing the thickness of electrodes by conventional slurry casting of more active materials on metal foils is a direct way to achieve the above goal.[11,12] However, it often suffers from poor electrochemical performance and weak mechanical stability with increasing electrode thickness and areal mass loading due to sluggish electron/ion transportation.[13,14] To address these limitations, novel three-dimensional (3D) electrodes with conductive porous structures are extensively explored, and diverse methods including magnetic,[15] wood templating,[16–18] freeze casting,[19–21] spark plasma sintering,[22] 3D printing,[23–25] wet calendaring,[26] and powder extrusion molding (PEM)[27] have been developed to increase the active material loading and enhance ion transportation. Take LiFePO$_4$ (LFP), the safest, cost-effective, and environmentally benign candidate material for commercial LIB cathodes, as an example, which has always been plagued with poor conductivity.[28,29] Kwon *et al.* incorporated LFP NPs onto multiwalled carbon nanotube (MWNT) modified cellulose textiles *via* an intricate ligand replacement reaction-mediated assembly, thus endowing the obtained conductive and porous cathode with a remarkable areal capacity (8.3 mA h cm^{-2} at 0.1C) and mechanical stability.[30] However, most abovementioned approaches are cumbersome, costly, and have difficulties for scale-up production. Therefore, for advanced high-performance batteries, it is essential to develop a facile and compatible method to redesign and rebuild the electrode structure to form new highly functional structures.

[a]Institute of Advanced Materials, Beijing Normal University, Beijing, 100875, China. E-mail: xiaoweizhang@bnu.edu.cn

[b]School of Chemistry, University of St Andrews, Fife KY16 9ST, St Andrews, UK

[c]Beijing Advanced Innovation Center for Materials Genome Engineering, Beijing Key Laboratory of Function Materials for Molecule & Structure Construction, School of Materials Science and Engineering, University of Science and Technology Beijing, Beijing, 100083, China

[d]Shunde Innovation School, University of Science and Technology Beijing, Shunde 528399, P. R. China

† Electronic supplementary information (ESI) available. See DOI: https://doi.org/10.1039/d3ta07139a

1736 | *J. Mater. Chem. A*, 2024, **12**, 1736–1745

This journal is © The Royal Society of Chemistry 2024

Here, we propose a novel *in situ* powder infiltration approach to embedding LFP nanoparticles into a porous aluminum network (pAlN) to fabricate an integrated 3D conductive scaffold-based electrode without using any binders. The aim is to work with active electrode materials (LFP active material) employed in commercial battery cells while re-designing the current collector (aluminum-based current collector) and binder structures and functions. The core focus is on optimizing the supporting elements to achieve better interfaces, improving ionic and electronic conductivity, optimizing pore structure and maximizing the availability of the active elements. Based on this design concept, the conductive pAlN substrate was prepared by sintering Al wool and Al powder with NaCl nanoparticles, and the porous 3D structure was formed *via* removing the NaCl template. The introduction of Al wool into Al foams strengthened the mechanical stability and electrical conductivity of the pAlN skeleton. The subsequent *in situ* powder infiltration treatment enabled the growth of very small LFP NPs between pre-added larger LFP nanoparticles and conductive pAlN substrates, which can act as binders and maximize the mass loading of active ingredients. In addition, the conductivity of the 3D electrode was further optimized by the introduction of small amounts of multi-walled carbon nanotubes (MWCNTs) and sucrose as carbon sources. Thanks to the Al-based continuous network skeleton and good interface, the resultant LFP/pAlN electrode achieved enhanced electronic/ionic conductivity and high areal capacity, and the underlying mechanism was demonstrated in detail.

2 Results and discussion

2.1 Design and fabrication of the 3D LFP/pAlN electrode

A key target of this work is to minimize the number and quantity of inactive components by converting conventional binders to multifunctional elements and improving interfaces. The design concept and fabrication process of the 3D LFP/pAlN electrode is schematically illustrated in Scheme 1. To begin with, the pAlN substrate (orange foam in Scheme 1a) was prepared *via* a sintering and dissolution process (SDP) and subsequent acid treatment.[31] Both Al wool and Al powder were used to form the mechanically reinforced and high-conductivity backbone, while ground NaCl powder was added as a pore-forming template. A small amount of Mg powder was used to enhance the sintering properties and increase the energy-absorbing capacity of the Al framework.[32] The powder mixture was hot pressed in N_2 (150 °C, 250 MPa), sintered at 500 °C, and then immersed in hot water to dissolve the NaCl template, obtaining the initial pAlN substrate (Fig. S1†). A 14 mm diameter mold was used for hot pressing to facilitate subsequent assembly and testing of the cell after loading with the active materials. The use of Al wool as the backbone of pAlN greatly improves its mechanical strength. The combination of high mechanical strength and high porosity of the pAlN substrate effectively inhibits the volume expansion and stress changes caused by further sintering and template removal. Then an acid treatment using 1 M HCl was applied to remove the impurities

(Fig. S2†), thus significantly reducing the resistance value of the pAlN skeleton from 3.12 kΩ to 2.5 Ω (Fig. S3†).
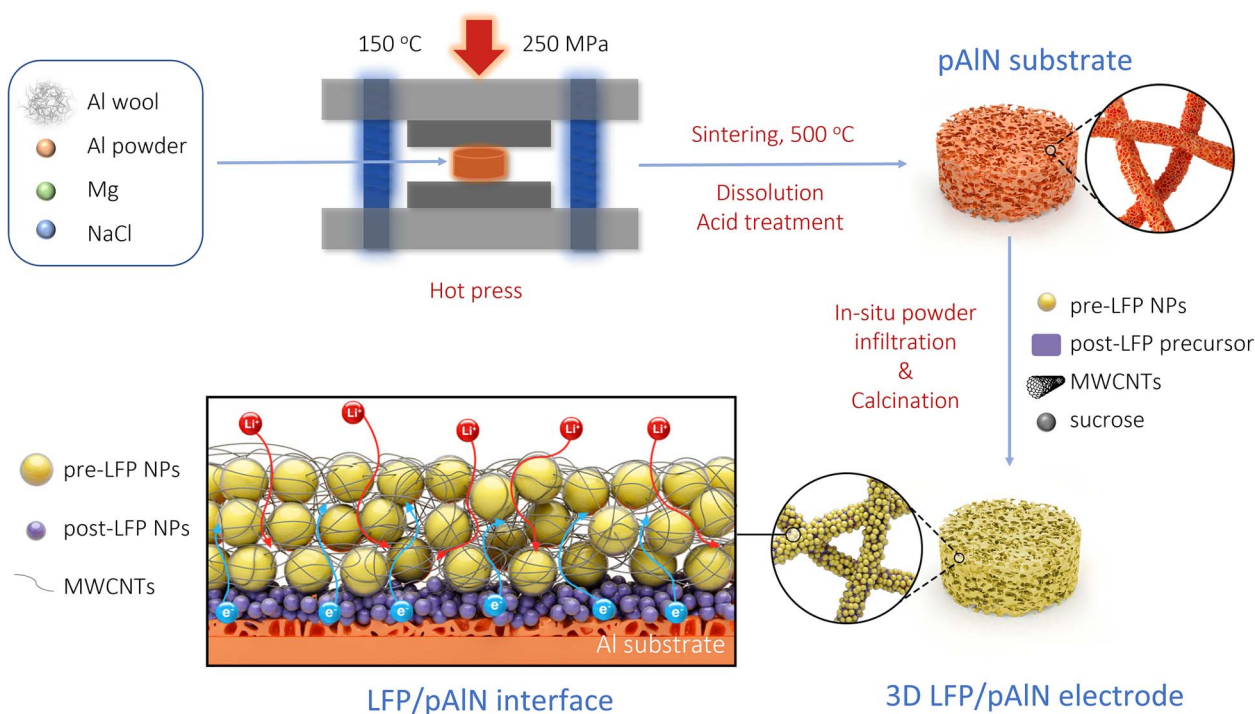
The 3D LFP/pAlN electrode (yellow foam in Scheme 1b) was prepared *via* an *in situ* powder infiltration method, using LFP precursor solution (mixture of $LiNO_3$, $Fe(NO_3)_3 \cdot 9H_2O$, $NH_4H_2PO_4$ and CTAB) and pre-added LFP NPs as raw materials. The pAlN substrate was dipped into the above infiltration solution and then calcined to form the post-synthesized LFP (post-LFP) nanoparticles. It is worth noting that the post-LFP nanoparticles (purple sphere in Scheme 1c) generated from *in situ* infiltration can function as a binder, connecting the pre-added LFP (pre-LFP) nanoparticles (yellow sphere in Scheme 1c) with the conductive pAlN substrate, thus enabling a close contact interface for enhanced electron transfer. During the *in situ* powder infiltration process, citric acid and cetyltrimethyl ammonium bromide (CTAB) were used as co-fuels and reducing agents for the synthesis of post-LFP NPs through the combustion process.[33,34] CTAB can also enhance the hydrophilicity of the pAlN substrate (Fig. S4†) and facilitate the growth of the active LFP components. Sucrose and MWCNTs were added as carbon sources to further enhance the conductivity of the 3D LFP/pAlN electrode. The infiltration and calcination process were repeated several times to obtain the 3D LFP/pAlN electrode with high mass loading of active LFP materials (Fig. S5†) incorporated into the conductive and mechanically stable skeleton.

The obtained hierarchical 3D LFP/pAlN electrode (Scheme 1c) consists of a conductive pAlN skeleton, pre-added LFP NPs, post-LFP NPs and a small amount of MWCNTs. The post-LFP NPs connected the conductive pAlN substrate with pre-added LFP NPs and MWCNTs. Compared to the traditional slurry-casting electrode, the 3D LFP/pAlN electrode provides several advantages: (i) the porous Al skeleton can maintain mechanical robustness. (ii) Multiple functions of the post-LFP NPs as both active materials and binders. (iii) The high mass loading of active LFP materials embedded into the hierarchically porous Al foam enables a high energy density of the electrode. (iv) The good mass transfer ability of porous 3D electrodes together with the connected conductive network of Al foam and carbon coating provide continuous ion and electron transfer pathways inside the 3D electrode. More importantly, the *in situ* powder infiltration method provides a novel manufacturing technique for direct growth of electrodes toward cost-effective and large-scale industrial production.

2.2 Morphology and microstructure of the 3D LFP/pAlN electrode

The morphology and microstructure of the 3D LFP/pAlN electrode were characterized by field-emission scanning electron microscopy (FESEM) and energy dispersive X-ray (EDX) spectroscopy. As shown in Fig. 1a–f, the low-magnification SEM image and corresponding EDX elemental mapping of the pAlN substrate show an interconnected porous network structure after the sintering and dissolution treatment of Al wool and Al particles, and the calculated porosity was estimated to be ~80% (Table S1†). The Si element detected from the EDX mapping

This journal is © The Royal Society of Chemistry 2024

J. Mater. Chem. A, 2024, **12**, 1736–1745 | 1737

Scheme 1 Schematic illustration of the synthesis of the 3D LFP/pAlN electrode.

image (Fig. 1d) is probably due to the final step of polishing the cross-section of pAlN. It can also be found that the introduction of Al wool is beneficial to enhance the long-range electronic conductivity and mechanical strength of Al foam. Moreover, the higher-magnification SEM image (Fig. 1g) discloses vertically packed nanosheets uniformly distributed on the surface of pAlN, further confirming the continuous network structure.

After *in situ* powder infiltration, as shown in Fig. 2a and S6,† the SEM and EDX images of the polished cross-section of LFP/pAlN display a large number of active LFP nanoparticles

grown on the surface of the pAlN substrate. The formation of orthorhombic olivine-type $LiFePO_4$ crystals was confirmed using the X-ray diffraction (XRD) patterns of the obtained 3D LFP/pAlN electrode (Fig. 2b), and no detectable impurity phase was observed.[35] To further clarify the growth of LFP nanoparticles on pAlN, the interface between active materials and the porous aluminum substrate was studied. As shown in Fig. 2c, the *in situ* formed post-LFP NPs with smaller size (<100 nm) can be clearly observed distributed between the aluminum nanosheets of the pAlN substrate and the pre-added large LFP
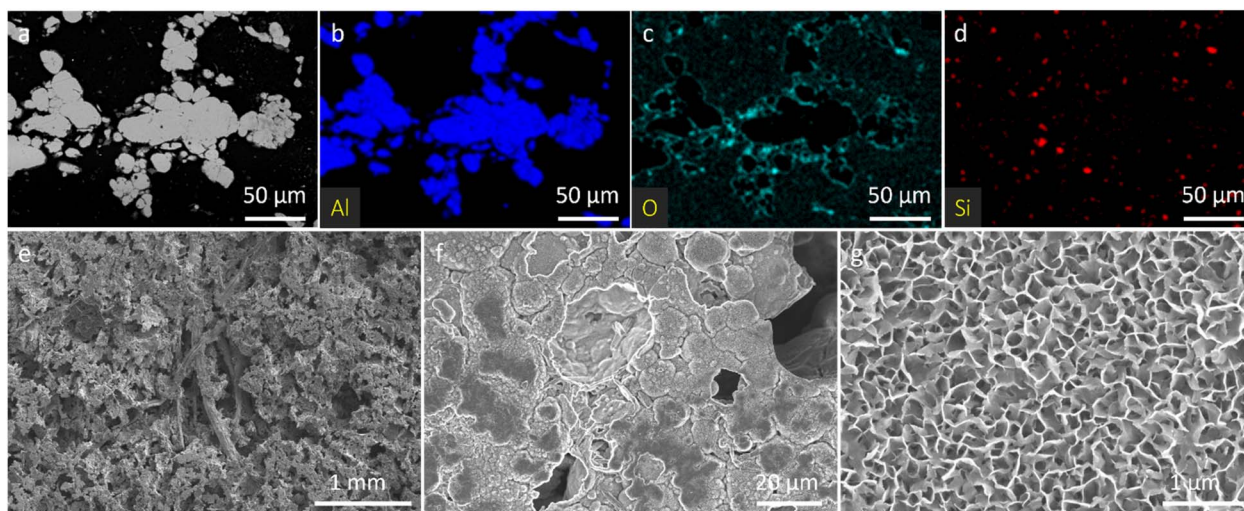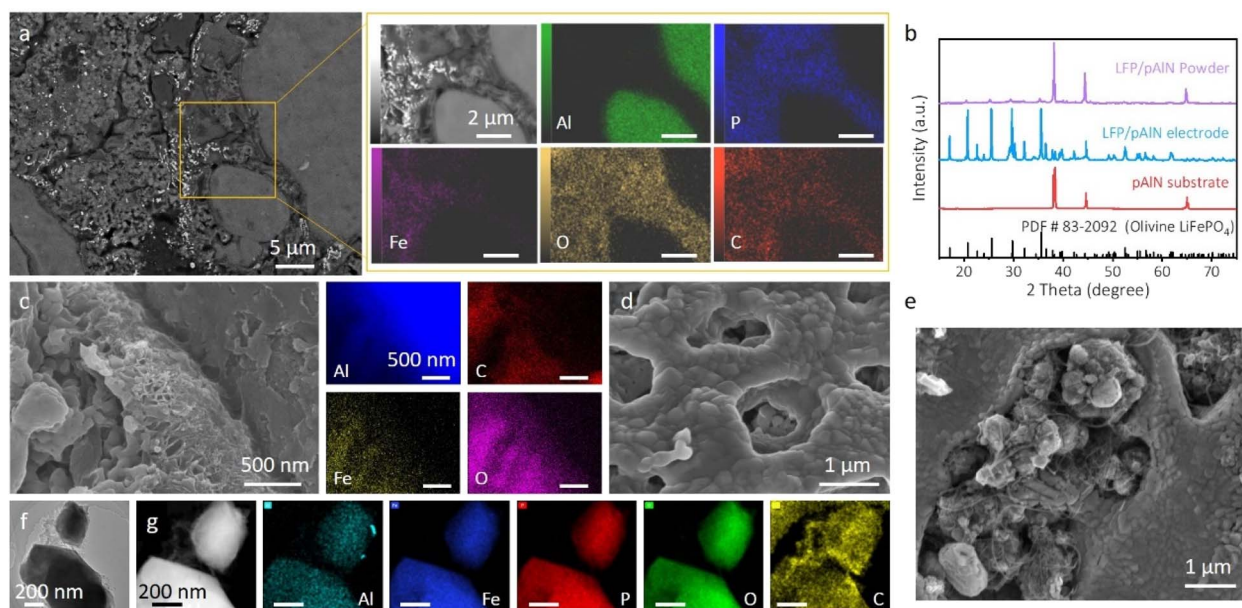

Fig. 1 (a) SEM image and (b–d) EDX elemental mapping images of the polished cross-section of the pAlN substrate. (e–g) SEM images of the non-polished surface of pAlN at different magnifications.

1738 | *J. Mater. Chem. A*, 2024, **12**, 1736–1745

This journal is © The Royal Society of Chemistry 2024

Fig. 2 (a) SEM image and EDX elemental mapping of the polished cross-section of the 3D LFP/pAlN electrode. (b) XRD patterns of the pAlN substrate, 3D LFP/pAlN electrode (monolithic electrode), and LFP/pAlN powder. (c–e) SEM image and EDX elemental mapping of the non-polished cross-section on the interface of the 3D LFP/pAlN electrode. (d and e) SEM images of the LFP/pAlN electrode surface at different positions. (f and g) TEM image, HAADF-STEM image, and EDX elemental mapping of connected LFP nanoparticles on the surface of the LFP/pAlN electrode.

NPs (∼200 nm), which avoids the use of binders and also increases the mass loading of the active LFP component. The porous structure of the connected LFP nanoparticles (Fig. 2d) was observed, which is attributed to fuel combustion (citric acid and CTAB) and gas evolution during the *in situ* powder infuriation process, resulting in a relatively fast mass transport channel for the Li$^+$ ions inside the electrode.[36]

The SEM images of non-polished LFP/pAlN (Fig. 2e) also show several MWCNTs wrapped around the active LFP NPs, which can promote the conductivity of the 3D electrodes. In line with the SEM and EDX results in Fig. 2a and c, we also notice uniform distribution of the carbon element in the LFP nanoparticle region, indicating that a conductive carbon coating was formed on the surface LFP nanoparticle. The transmission electron microscope (TEM) images (Fig. 2f and S7†), high angle annular dark field-scanning transmission electron microscope (HAADF-STEM) image (Fig. 2g) and the corresponding elemental mapping of the LFP particles sheared and ground from the 3D LFP/pAlN electrode further confirm the carbon coating and carbon connecting between the LFP nanoparticles, which may be attributed to the strong chelation between citric acid and metal ions during the *in situ* powder infiltration process.[37,38] The connected carbon-coated LFP nanoparticles and their close contact with the pAlN substrate provide a continuous electron transport pathway, thus boosting the electronic conductivity and efficiency of the 3D LFP/pAlN electrode. In addition, as shown in Fig. 2f and g, an evenly distributed Al element throughout the LFP NPs can be observed, which may be attributed to the etching of Al species of pAlN by the acidic precursor solution containing citric acid.

Calcination treatment during the *in situ* powder infiltration process is crucial to construct the 3D LFP/pAlN electrode, which contains a pre-heating step at 230 °C in air of the precursor mixture and a sintering step at 600 °C under a hydrogen–argon atmosphere. We carried out thermogravimetric analysis (TGA) to investigate the composition evolution and material stability during the calcination process. As shown in Fig. 3a, the TGA curve of pre-added LFP NPs shows an obvious mass increase when heating the material up to 300 °C in air, which may stem from the oxidation of LFP. Considering that the pre-heating temperature of the precursor mixture was set at 230 °C, the relative stability of pre-added LFP during the *in situ* powder infiltration process can be ensured. Compared to pre-LFP NPs, the TGA of the LFP/pAlN electrode shows a weight loss of ∼9.2 wt% at temperature above 600 °C.[39] This weight loss can be attributed to the carbon release from the additive components in the precursor mixture, which was further confirmed from the TGA curves of CTAB, citric acid, sucrose, and MWCNTs (Fig. S8†).[40] Notably, during the pre-heating treatment at 230 °C in air, the added CTAB as surfactant and citric acid as a chelating agent were mostly decomposed, indicating that the connected carbon coating in the LFP/pAlN electrode is mainly due to the contribution of sucrose. The phase structure and carbon coating in the 3D LFP/pAlN electrode were further confirmed by Raman and Fourier transform infrared (FT-IR) spectroscopy. The Raman peak at around 950 cm^{-1} (Fig. 3b) was related to the internal stretching vibration of PO$_4^{3-}$, which is consistent with the FT-IR spectra (Fig. 3c), confirming the existence of the active LiFePO$_4$ component.[41] The strong Raman peaks centered at 1347 and 1591 cm^{-1} can be assigned to type D and type G bands

This journal is © The Royal Society of Chemistry 2024

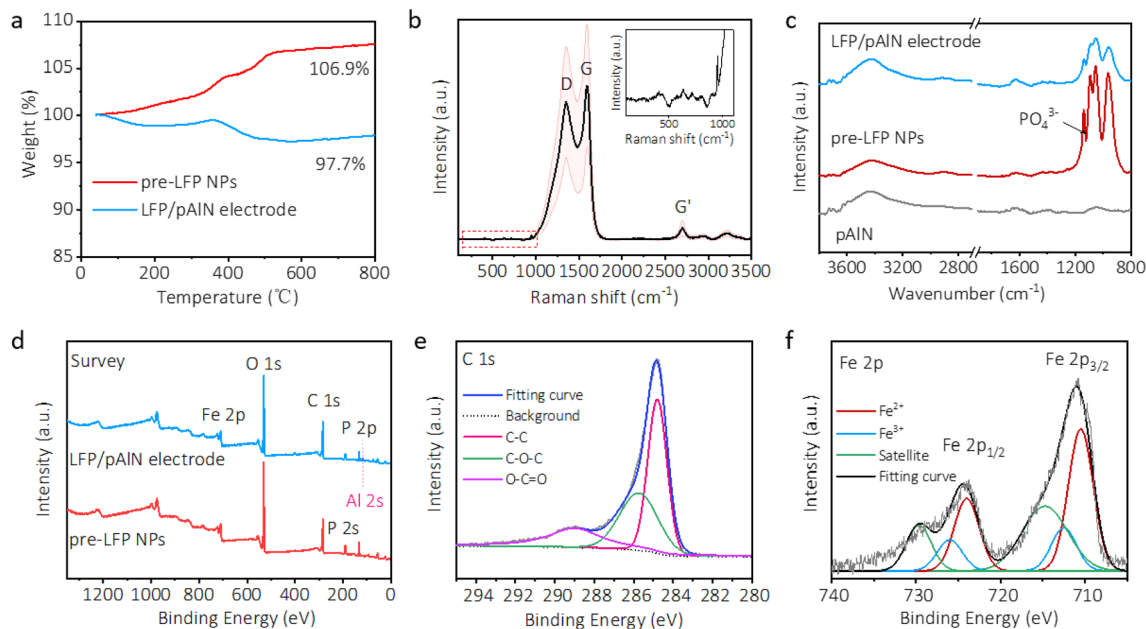*J. Mater. Chem. A*, 2024, **12**, 1736–1745 | **1739**

Fig. 3 (a) TGA curves of pre-LFP NPs and the 3D LFP/pAlN electrode measured under an air atmosphere. (b) Raman spectrum of the 3D LFP/pAlN electrode, the inset shows the detail of Raman spectrum under 1200 cm^{-1}. (c) FT-IR spectra of the pAlN substrate, pre-LFP NPs and 3D LFP/pAlN electrode. (d) XPS survey of pre-LFP NPs and the 3D LFP/pAlN electrode. High-resolution XPS spectra of (e) C 1s and (f) Fe 2p for the 3D LFP/pAlN electrode.

of carbon species, respectively.[21] Notably, the intensity ratio of the D-to-G band was estimated to be 0.89, suggesting the graphitic carbon coating in the 3D LFP/pAlN electrode for better electron transfer. In addition, the porosity of the pAlN substrate and the 3D electrodes was investigated using Brunauer–Emmett–Teller (BET) specific surface area and pore size distribution (Fig. S9, Table S2†). After the loading of the LFP particles, the specific surface area of the 3D electrode decreased, while the number of pores with larger sizes was increased, possibly due to the gas leakage during the sintering process, which is more conducive to the transport of electrolytes.

To further demonstrate the composition and valence state of the 3D LFP/pAlN electrode, X-ray photoelectron spectroscopy (XPS) was conducted. The survey XPS spectrum of the 3D LFP/pAlN electrode (Fig. 3d) shows the co-existence of Fe, P, C, O, and Al species, which is in accordance with the elemental distribution in EDX mapping (Fig. 2 and S6†). As shown in Fig. 3e, the C 1s spectrum shows a strong asymmetric peak of C–C at 284.6 eV, and two relatively weak peaks located at 286 eV and 289 eV that can be assigned to C–O–C and O–C=O, respectively.[42] Combining the above results of morphology and structure characterization, it can be inferred that the carbon coating on the LFP nanoparticles and carbon connecting among LFP NPs in the 3D electrode were confirmed, which mainly derived from the decomposition of sucrose during the sintering treatment in the *in situ* powder infiltration process. The high-resolution Fe 2p spectrum (Fig. 3f) shows two splitting peaks at 710.5 eV and 724 eV with corresponding "shake-up" satellite peaks, and the binding energy separation between the two peaks was about 13.5 eV, which can be assigned to Fe 2p$_{3/2}$ and Fe 2p$_{1/2}$ caused by spin–orbit coupling.[43] This result suggests

the characteristic Fe^{2+} valence state of olivine-type LiFePO$_4$ in the 3D LFP/pAlN electrode, which is consistent with previous research.[44,45] Moreover, the weak signals for Fe^{3+} valence state (712.5 eV and 726 eV) related to FePO$_4$ were observed, representing characteristic peaks of LiFePO$_4$ olivine as well. Compared with the XPS spectra of commercial carbon-coating LFP nanoparticles (Fig. S10†), the valence states of C, Fe, P and O (Fig. S11†) elements of the 3D LFP/pAlN electrode are well maintained, indicating the good olivine crystal phase of LiFePO$_4$, which is crucial for achieving high-performance electrodes.

2.3 Battery performance of the 3D LFP/pAlN electrode

The electrochemical performance of the 3D LFP/pAlN electrode was investigated by galvanostatic charge/discharge (GCD) and electrochemical impedance spectroscopy (EIS) measurements. Fig. 4a shows the GCD profiles of the 3D LFP/pAlN electrodes prepared with solutions of different compositions and concentrations by the *in situ* powder infiltration method. Note that before testing a standard infiltration solution consists of pre-LFP NPs (0.5 g), post-LFP precursor (mixture of LiNO$_3$, Fe(NO$_3$)$_3$·9H$_2$O, NH$_4$H$_2$PO$_4$ and CTAB), sucrose, MWCNTs and citric acid (Scheme 1b). The infiltration cycle was set to 7 times for better comparison. As shown in Fig. 4a, compared to control experiments without pre-LFP NPs or without the post-LFP precursor, the 3D LFP LFP/pAlN electrode using 0.5 M post-LFP precursor solution exhibits the best performance with a high mass loading (LFP nanoparticles and carbon coating) of 65 mg cm^{-2}. The 3D electrode prepared with excessive post-LFP precursor (1 M) shows a decrease in specific capacity, possibly

1740 | J. Mater. Chem. A, 2024, 12, 1736–1745

This journal is © The Royal Society of Chemistry 2024
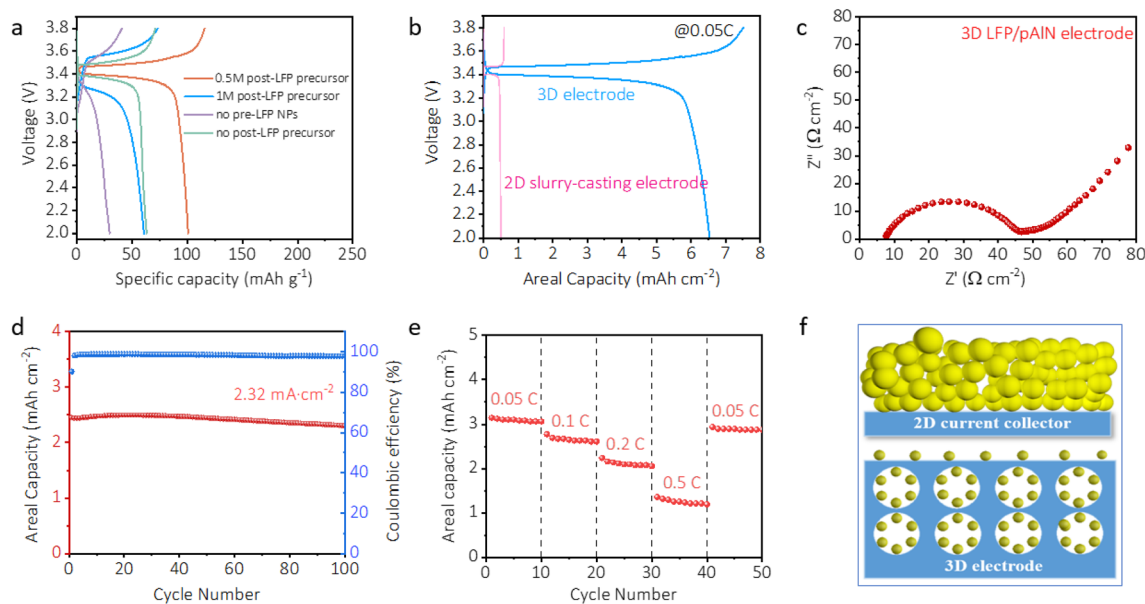
Fig. 4 (a) Galvanostatic charge/discharge profiles of the 3D LFP/pAlN electrode using different infiltration solution. (b) Areal capacity of the 3D LFP/pAlN electrode and conventional 2D slurry-casting electrode. (c) Nyquist plot of the 3D LFP/pAlN electrode. (d) Traces of the areal capacity and coulombic efficiency of the 3D LFP/pAlN electrode as a function of GCD cycles at 2.32 mA cm^{-2}. (e) Rate performance of the 3D LFP/pAlN electrode. (f) Schematic comparison of the 3D LFP/pAlN electrode and the 2D slurry-casting electrode.

due to the poorer crystallinity of post-LFP NPs than the pre-added LFP species resulting from a relatively lower sintering temperature. These results indicate that the pre-LFP NPs with good crystallization make a major contribution to the electrode efficiency, while the post-LFP NPs generated from the precursor not only increase the mass loading of active components but also enhance the overall electrochemical performance as a functional binder. The GCD profile of the 3D LFP/pAlN electrode with 0.5 M post-LFP precursor shows a typical charge–discharge plateau around 3.4 V with a specific capacity of 101 mA h g^{-1}. The areal capacity of the 3D LFP/pAlN electrode (Fig. 1b) was estimated to be 6.56 mA h cm^{-2} (areal current density: 0.55 mA cm^{-2}), much better than that of the conventional 2D slurry-casting electrode with an active LFP mass loading of 2.6 mg cm^{-2} on the Al foil collector, and superior to those of the recently reported novel structural 3D electrodes using non-situ growth methods (Table S3†) and *in situ* grown 3D electrodes with porous and conductive substrates (Table S4†).[30,46–49] In particular, the 3D LFP/pAlN electrode in this study also has significant advantages of cost-effectiveness and scale-up production compared to the reported electrodes.

The type and amount of organic fuels (citric acid, urea, glycine and CTAB), which can chelate the cations in the post-LFP precursor and affect the microstructure of post-LFP NPs, were investigated to optimize the electrode performance.[50] As shown in Fig. S12a,† the GCD profile of the 3D LFP/pAlN electrode prepared using citric acid–CTAB mixed fuel shows superior specific capacity compared with that of using urea–CTAB and glycine–CTAB fuels, indicating a more suitable combustion rate and better physicochemical properties were achieved by mixing citric acid and CTAB. Fig. S12b† shows that a certain amount of CTAB, which can

facilitate the infiltration of the precursor solution and enable a higher mass loading of the active LFP material (Fig. S4†), boosted the electrochemical performance. However, excessive CTAB inhibited the dispersion of LFP particles in 3D aluminum foam, resulting in reduced efficiency.

EIS analysis was conducted to investigate the reaction kinetics. As shown in Fig. 4c, the Nyquist plot of the LFP/pAlN electrode exhibits a single depressed semicircle with a relatively smaller radius in the high frequency region, which can be ascribed to the lower charge-transfer resistance (R_{ct}), confirming the fast electron and ion transport of the 3D LFP/pAlN electrode. The cycling performance was determined at a relatively high areal current density of ~2.32 mA cm^{-2} to investigate the stability of the electrodes. As shown in Fig. 4d, after 100 cycles, the 3D LFP/pAlN electrode exhibits a capacity retention of 94.1% with a high coulombic efficiency of 97.9%, indicating a good long-term electrochemical stability, which can be attributed to the enhanced mechanical properties and robust continuous framework of the electrode. The XRD plot (Fig. S13†) and SEM images (Fig. S14†) of the 3D LFP/pAlN electrode after 100 charge–discharge cycles compared well with the initial ones, further confirming the good structure and morphology stability. The current density-dependent GCD measurements for the 3D LFP/pAlN electrodes were conducted at various current densities (Fig. 4e) to evaluate the rate performance. The areal capacities of the 3D LFP/pAlN electrode gradually decreased with increasing rate from 0.05C to 0.5C, which is due to the insufficient ion diffusion kinetics originating from the long ion transport distance in irregularly connected pores. Fig. 4f further illustrates the advantage of the 3D LFP/pAlN electrode, which can be assigned to the *in situ* incorporation of active materials within a 3D porous conductive

This journal is © The Royal Society of Chemistry 2024

J. Mater. Chem. A, 2024, **12**, 1736–1745 | **1741**

network, thus reducing the thickness of active materials, enlarging the contact area of interfaces among the aluminum substrate, active LFP materials and electrolyte, thus enhancing the electron transport and shortening the diffusion pathways of Li^+ ions.[36] In addition, we should note that the mass loading of the 3D LFP/pAlN electrode can be adjusted by the infiltration times (Fig. S5†), which can provide a cost-effective and large-scale industrial manufacturing process and inspire ideas for the development of next-generation high areal capacity electrodes.

3 Conclusions

In summary, we have proposed a low-cost and scale-up *in situ* powder infiltration method to fabricate novel binder-free 3D LFP/pAlN with high mass loading of active materials, porous mass transfer channels, and conductive electron transport pathways, thus enabling a high areal capacity and good mechanical stability of the 3D positive electrode. The obtained pAlN substrate possesses a high porosity of 80% with an aluminum-based continuous network skeleton and an assembled surface of vertically grown nanosheets. The *in situ* grown post-LFP NPs with a good carbon coating and connecting function as a binder to bridge the pre-LFP NPs and the pAlN substrate, providing high LFP mass loading and facilitating the electron/ion transport inside the 3D electrode. Benefiting from the structural merits, the 3D LFP/pAlN electrode exhibits a high areal capacity of 6.56 mA h cm^{-2} (at 0.55 mA cm^{-2}) and excellent cycling performance (94.1%) at an areal current density of 2.32 mA cm^{-2} for 100 cycles. This study develops a facile and novel strategy for constructing binder-free 3D electrodes with high areal capacity, which integrates multiple functionalities with cost-effectiveness and scalability and sheds light on designing of next-generation electronic devices.

4 Methods

4.1 Preparation of the pAlN substrate

The pAlN substrate was prepared using the sintering dissolution process with minor modifications.[31,32] Al powder (99.99% purity) and ground NaCl powder were used as the matrix materials and template, and a small amount of magnesium powder was added to absorb the trapped air and reduce the surface oxidation of Al particles. Typically, 210 mg of NaCl powder, 70 mg of Al powder, and 0.9 mg Mg powder were mixed. 20 mg of Al wool (Lustersheen) and the above powder mixture were poured into a cylindrical mold with a diameter of 14 mm, and hot pressed (PP-600DG, Tianjin Jingtuo Co., Ltd) at 150 °C under a pressure of 250 MPa. The Al wool was used as a skeleton to improve the mechanical stability and electrical conductivity of the Al foam. The obtained sample was sintered in a furnace in N_2 at 500 °C for 2 h, and then put in warm deionized water for 2 h to dissolve the NaCl template. After washing with deionized water and drying, the initial Al substrate was treated with 1 M HCl for 30 min to remove the impurities. Finally, the porous Al network (pAlN) substrate was obtained after further washing with deionized water and drying.

4.2 Preparation of the infiltration solution

Typically, stoichiometric amounts of 5 mmol of lithium nitrate ($LiNO_3$), iron(III) nitrate hydrate ($Fe(NO_3)_3 \cdot 9H_2O$), and ammonium dihydrogen phosphate ($NH_4H_2PO_4$) were dissolved in 10 mL deionized water. Then 7.5 mmol citric acid, 1 g sucrose and 0.15 g CTAB were added to the solution. After stirring for 30 min, 10 mg of multi-walled carbon nanotubes (MWCNTs, Chengdu Organic Chemicals Co. Ltd) as the conductive additive and 0.5 g LiFePO$_4$ (pre-LFP) active material were added to the solution. After stirring for 24 h, the infiltration solution was obtained.

4.3 Preparation of the 3D LFP/pAlN electrode

The 3D LFP/pAlN electrode was prepared *via* a modified *in situ* powder infiltration method. First, the as-prepared pAlN substrate was fully dipped in the above infiltration solution, well stirred, and dried at 80 °C in an oven. The LiFePO$_4$ precursor gel was obtained within the pores of pAlN. Then the sample was calcined in an oven at 230 °C for the combustion step.[50,51] To obtain the 3D LFP/pAlN electrode with high mass loading of the active LFP material, the powder infiltration and calcination processes were repeated several times. During the subsequent cyclic infiltration process, the dipping step was replaced by dropwise addition of the LFP precursor solution to avoid impurities. Then the 3D LFP/pAlN electrode was achieved by sintering at 600 °C for 8 h under a hydrogen (5% volume)–argon atmosphere with a heating rate of 3 °C min^{-1}. The electrodes are subsequently placed in an argon-filled glove box for further use.

4.4 Preparation of the traditional 2D electrode

The traditional 2D electrodes were fabricated by using commercial LiFePO$_4$ nanoparticles as the active material, conductive carbon black (Super-P) and polyvinylidene fluoride (PVDF) binder in a weight ratio of 7 : 2 : 1. They were mixed in a mortar for 1 h and then dispersed in *N*-methyl-2-pyrrolidone (NMP) to form a homogeneous slurry. The slurry was coated on aluminum foil and dried in a vacuum oven at 120 °C for 10 h. The thickness of the active material on the 2D electrode was increased to 750 μm in order to optimize the loading capacity while ensuring stability. The electrode sheet is subsequently transformed into a small circular shape (areal mass loading: ~2.6 mg cm^{-2}) and reserved for utilization within an argon-filled glove box.

4.5 Materials characterization

Powder X-ray diffraction was performed on a Bruker D8 Advance X-ray diffractometer using Cu Kα radiation ($\lambda = 0.154$ nm). Field-emission scanning electron microscopy (FESEM) images were obtained using a Regulus 8100 working at 5 kV. Transmission electron microscope (TEM) images, high-angle annular dark-field scanning transmission electron microscopy (HAADF-STEM) images and the EDX mapping images were recorded using an FEI Talos F200S high-resolution transmission electron microscope working at 200 kV. Fourier transform infrared

1742 | *J. Mater. Chem. A*, 2024, **12**, 1736–1745

This journal is © The Royal Society of Chemistry 2024

spectra (FTIR) were acquired using a Nicolet 6700 FT-IR spectrometer. The thermogravimetric analysis (TGA) was carried out using a METTLER TOLEDO TGA/DSC3+ instrument with a heating rate of 10 °C min^{-1} in air. X-ray photoelectron spectroscopy (XPS) measurements were performed on an ESCALAB 250Xi X-ray photoelectron spectrometer using a monochromatic Al Kα (1486.6 eV) X-ray source. The Raman spectra of the electrodes were acquired using a Renishaw inVia™ confocal Raman microscope system, equipped with a Leica microscope and focused through a 50× objective lens, and a 532 nm excitation laser with a power of 0.5 mW (1% intensity) was employed.

4.6 Electrochemical testing

The 3D LFP/pAlN electrodes were evaluated with a standard CR2032 coin cell coupled with Li foil as the anode using the electrolyte of 1.0 M LiPF$_6$ in EC : DMC : EMC = 1 : 1 : 1 vol% with a glass fiber separator (Whatman). For a single electrode, different amounts of electrolyte were used for the 2D electrode (60–100 μL) and the 3D LFP/pAlN electrode (180 μL). All cells were fabricated in an argon-filled glove box. The cells were aged for 12 h before charge/discharge tests. The electrochemical properties of 3D LFP/pAlN electrodes were subsequently evaluated within a cut-off potential voltage range of 2 to 3.8 V vs. Li/Li$^+$, using the galvanostatic charge/discharge mode in a Land Instruments testing system (Land CT3001A). For the long-term cycling, the cells were subjected to constant charge and discharge at 0.5C for the following cycles. The areal capacities of the electrodes were determined by dividing the measured cell capacity by the geometric electrode area ($\sim$1.54 cm^2). The electrochemical impedance spectroscopy (EIS) measurements were conducted using an E200 three-electrode battery test cell through a Princeton PMC 1000&500 electrochemical workstation with a frequency range of 100 kHz $\sim$0.1 Hz and a voltage amplitude of 10 mV.

Data availability

The research data supporting this publication can be accessed at https://doi.org/10.17630/92c60482-1975-4933-ace5-91380b9b8ae2.[52]

Author contributions

X. W. Z., J. T. S. I. and G. W. conceived and supervised the project. X. W. Z. and Z. Y. Z. designed the study, performed the experiments and wrote the paper. X. W. Z., Z. Y. Z. and J. T. S. I. analyzed the results and revised the manuscript. P. W., I. M. P. and H. Y. G. participated in material characterization. All authors discussed the results and commented on the paper.

Conflicts of interest

The authors declare no conflict of interest.

Acknowledgements

Notes and references

1 Y. Liu, *et al.*, Roll-to-roll solvent-free manufactured electrodes for fast-charging batteries, *Joule*, 2023, **7**, 952–970.

2 J. Xu, J. Lei, N. Ming, C. Zhang and K. Huo, Rational design of wood-structured thick electrode for electrochemical energy storage, *Adv. Funct. Mater.*, 2022, **32**, 2204426.

3 T. P. Plateau, H. Pham, Y. Zhu, M. Leu and J. Park, Enabling ultrathick electrodes via a microcasting process for high energy and power density lithium-ion batteries, *Adv. Energy Mater.*, 2022, **12**, 2201353.

4 N. Nitta, F. Wu, J. T. Lee and G. Yushin, Li-ion battery materials: present and future, *Mater. Today*, 2015, **18**, 252–264.

5 F. Wu, *et al.*, High-mass-loading electrodes for advanced secondary batteries and supercapacitors, *Electrochem. Energy Rev.*, 2021, **4**, 382–446.

6 X. Fu, *et al.*, Rethinking the electrode multiscale microstructures: a review on structuring strategies toward battery manufacturing genome, *Adv. Energy Mater.*, 2023, 2301385.

7 A. M. Boyce, *et al.*, Design of scalable, next-generation thick electrodes: opportunities and challenges, *ACS Nano*, 2021, **15**, 18624–18632.

8 Y. Chen, B. Zhao, Y. Yang and A. Cao, Toward high-areal-capacity electrodes for lithium and sodium ion batteries, *Adv. Energy Mater.*, 2022, **12**, 2201834.

9 L. Zhang, *et al.*, Advanced matrixes for binder-free nanostructured electrodes in lithium-ion batteries, *Adv. Mater.*, 2020, **32**, 1908445.

10 Y. Kuang, C. Chen, D. Kirsch and L. Hu, Thick electrode batteries: principles, opportunities, and challenges, *Adv. Energy Mater.*, 2019, **9**, 1901457.

11 S.-H. Park, *et al.*, High areal capacity battery electrodes enabled by segregated nanotube networks, *Nat. Energy*, 2019, **4**, 560–567.

12 Y. Guo, *et al.*, Visualization of concentration polarization in thick electrodes, *Energy Storage Mater.*, 2022, **51**, 476–485.

13 J. Wu, *et al.*, From fundamental understanding to engineering design of high-performance thick electrodes for scalable energy-storage systems, *Adv. Mater.*, 2021, **33**, 2101275.

14 M. Zhang, *et al.*, Coupling of multiscale imaging analysis and computational modeling for understanding thick cathode degradation mechanisms, *Joule*, 2023, **7**, 201–220.

This journal is © The Royal Society of Chemistry 2024

J. Mater. Chem. A, 2024, **12**, 1736–1745 | **1743**

15 J. Billaud, F. Bouville, T. Magrini, C. Villevieille and A. R. Studart, Magnetically aligned graphite electrodes for high-rate performance Li-ion batteries, *Nat. Energy*, 2016, **1**, 16097.

16 C. Chen, *et al.*, Highly conductive, lightweight, low-tortuosity carbon frameworks as ultrathick 3D current collectors, *Adv. Energy Mater.*, 2017, **7**, 1700595.

17 L.-L. Lu, *et al.*, Wood-inspired high-performance ultrathick bulk battery electrodes, *Adv. Mater.*, 2018, **30**, 1706745.

18 F. Wang, *et al.*, Inspired by wood: thick electrodes for supercapacitors, *ACS Nano*, 2023, **17**, 8866–8898.

19 S. Deville, The lure of ice-templating: recent trends and opportunities for porous materials, *Scr. Mater.*, 2018, **147**, 119–124.

20 K. Yang, *et al.*, Constructing a highly efficient aligned conductive network to facilitate depolarized high-areal-capacity electrodes in Li-ion batteries, *Adv. Energy Mater.*, 2021, **11**, 2100601.

21 Z. Zhao, *et al.*, Sandwich, vertical-channeled thick electrodes with high rate and cycle performance, *Adv. Funct. Mater.*, 2019, **29**, 1809196.

22 R. Elango, A. Demortière, V. De Andrade, M. Morcrette and V. Seznec, Thick binder-free electrodes for Li–ion battery fabricated using templating approach and spark plasma sintering reveals high areal capacity, *Adv. Energy Mater.*, 2018, **8**, 1703031.

23 J. Wang, *et al.*, Toward high areal energy and power density electrode for Li-ion batteries via optimized 3D printing approach, *ACS Appl. Mater. Interfaces*, 2018, **10**, 39794–39801.

24 T.-S. Wei, B. Y. Ahn, J. Grotto and J. A. Lewis, 3D printing of customized Li-ion batteries with thick electrodes, *Adv. Mater.*, 2018, **30**, 1703027.

25 M. Zhang, *et al.*, A 3D-printed proton pseudocapacitor with ultrahigh mass loading and areal energy density for fast energy storage at low temperature, *Adv. Mater.*, 2023, **35**, 2209963.

26 J. Wu, *et al.*, Building efficient ion pathway in highly densified thick electrodes with high gravimetric and volumetric energy densities, *Nano Lett.*, 2021, **21**, 9339–9346.

27 M. E. Sotomayor, *et al.*, Ultra-thick battery electrodes for high gravimetric and volumetric energy density Li-ion batteries, *J. Power Sources*, 2019, **437**, 226923.

28 J. Wang and X. Sun, Olivine LiFePO4: the remaining challenges for future energy storage, *Energy Environ. Sci.*, 2015, **8**, 1110–1138.

29 R. Malik, F. Zhou and G. Ceder, Kinetics of non-equilibrium lithium incorporation in $LiFePO_4$, *Nat. Mater.*, 2011, **10**, 587–590.

30 M. Kwon, *et al.*, Textile-type lithium-ion battery cathode enabling high specific/areal capacities and high rate capability through ligand replacement reaction-mediated assembly, *Adv. Energy Mater.*, 2021, **11**, 2101631.

31 Y. Zhao, F. Han and T. Fung, Optimisation of compaction and liquid-state sintering in sintering and dissolution process for manufacturing Al foams, *J. Mater. Sci. Eng. A*, 2004, **364**, 117–125.

32 D. X. Sun and Y. Y. Zhao, Static and dynamic energy absorption of Al foams produced by the sintering and dissolution process, *Metall. Mater. Trans. B*, 2003, **34**, 69–74.

33 P. A. Connor, *et al.*, Tailoring SOFC electrode microstructures for improved performance, *Adv. Energy Mater.*, 2018, **8**, 1800120.

34 A. Varma, A. S. Mukasyan, A. S. Rogachev and K. V. Manukyan, Solution Combustion synthesis of nanoscale materials, *Chem. Rev.*, 2016, **116**, 14493–14586.

35 Y. Zhao, L. Peng, B. Liu and G. Yu, Single-crystalline $LiFePO_4$ nanosheets for high-rate Li-ion batteries, *Nano Lett.*, 2014, **14**, 2849–2853.

36 S. Jin, Y. Jiang, H. Ji and Y. Yu, Advanced 3D current collectors for lithium-based batteries, *Adv. Mater.*, 2018, **30**, 1802014.

37 G. Xie, H.-J. Zhu, X.-M. Liu and H. Yang, A core–shell $LiFePO_4$/C nanocomposite prepared via a sol–gel method assisted by citric acid, *J. Alloys Compd.*, 2013, **574**, 155–160.

38 Y. Wang, *et al.*, An interconnected $NaTi_2(PO_4)_3$/carbon composite from an all-integrated framework with chelating Ti in a cross-linked citric acid-organic phosphonic acid skeleton for high-performance sodium storage, *J. Colloid Interface Sci.*, 2022, **626**, 1–12.

39 I. Belharouak, C. Johnson and K. Amine, Synthesis and electrochemical analysis of vapor-deposited carbon-coated $LiFePO_4$, *Electrochem. Commun.*, 2005, **7**, 983–988.

40 X. Wang, *et al.*, Graphene-decorated carbon-coated $LiFePO_4$ nanospheres as a high-performance cathode material for lithium-ion batteries, *Carbon*, 2018, **127**, 149–157.

41 E. Markevich, *et al.*, Raman spectroscopy of carbon-coated $LiCoPO_4$ and $LiFePO_4$ olivines, *J. Power Sources*, 2011, **196**, 6433–6439.

42 R. Dedryvère, *et al.*, X-Ray Photoelectron Spectroscopy Investigations of Carbon-Coated Li_xFePO_4 Materials, *Chem. Mater.*, 2008, **20**, 7164–7170.

43 J. Jiang, W. Liu, J. Chen and Y. Hou, $LiFePO_4$ nanocrystals: liquid-phase reduction synthesis and their electrochemical performance, *ACS Appl. Mater. Interfaces*, 2012, **4**, 3062–3068.

44 J. Tu, K. Wu, H. Tang, H. Zhou and S. Jiao, Mg–Ti co-doping behavior of porous $LiFePO_4$ microspheres for high-rate lithium-ion batteries, *J. Mater. Chem. A*, 2017, **5**, 17021–17028.

45 K. Zaghib, A. Mauger, F. Gendron and C. M. Julien, Surface effects on the physical and electrochemical properties of thin $LiFePO_4$ particles, *Chem. Mater.*, 2008, **20**, 462–469.

46 H. Sun, *et al.*, Three-dimensional holey-graphene/niobia composite architectures for ultrahigh-rate energy storage, *Science*, 2017, **356**, 599–604.

47 S. Zhou, *et al.*, Sub-thick electrodes with enhanced transport kinetics via in situ epitaxial heterogeneous interfaces for high areal-capacity lithium ion batteries, *Small*, 2021, **17**, 2100778.

48 Y. Ham, *et al.*, 3D periodic polyimide nano-networks for ultrahigh-rate and sustainable energy storage, *Energy Environ. Sci.*, 2021, **14**, 5894–5902.

49 X. Yu, *et al.*, A dual-carbon-anchoring strategy to fabricate flexible $LiMn_2O_4$ cathode for advanced lithium-ion

1744 | *J. Mater. Chem. A*, 2024, **12**, 1736–1745

This journal is © The Royal Society of Chemistry 2024

batteries with high areal capacity, *Nano Energy*, 2020, **67**, 104256.

50 Z. Li, *et al.*, Controlled hydrothermal/solvothermal synthesis of high-performance LiFePO$_4$ for Li-ion batteries, *Small Methods*, 2021, **5**, 2100193.

51 M. Karami, S. M. Masoudpanah and H. R. Rezaie, Solution combustion synthesis of hierarchical porous LiFePO$_4$ powders as cathode materials for lithium-ion batteries, *Adv. Powder Technol.*, 2021, **32**, 1935–1942.

52 Z. Zhao, X. Zhang, P. Wang, I. M. Pateli, H. Gao, G. Wang, J. T. S. Irvine, New approaches to three-dimensional positive electrodes enabling scalable high areal capacity, *Dataset*, University of St Andrews Research Portal, 2023, DOI: **10.17630/92c60482-1975-4933-ace5-91380b9b8ae2**.

This journal is © The Royal Society of Chemistry 2024

J. Mater. Chem. A, 2024, **12**, 1736–1745 | **1745**